

Deformation-induced crystallization in amorphous Al₈₅Ni₁₀La₅ alloy

Jens Vierke^a, Gerhard Schumacher^a, Vitaly P. Pilyugin^b, Ingwer A. Denks^a, Ivo Zizak^a,

Christian Wolf^a, Nelia Wanderka^a, Markus Wollgarten^a, John Banhart^a

^a Helmholtz Center Berlin for Materials and Energy, D-14109 Berlin

^b Ural Branch of the Russian Academy of Sciences, Kovalevray street 18, 620219

Yekaterinburg, Russia

Abstract

Helium-atomized amorphous Al₈₅Ni₁₀La₅ (at.-%) powder was investigated in the as-atomized state and after consolidation at room temperature using high pressure torsion. The samples were investigated by scanning electron microscopy, in-situ and ex-situ angle-dispersive X-ray diffractometry (XRD), ex-situ energy-dispersive XRD, differential scanning calorimetry, and inductively coupled plasma mass spectroscopy. The as-atomized powder shows a glass transition and subsequent crystallization of fcc-Al and intermetallic phases within a narrow temperature range upon continuous heating. Primary crystallization of fcc-Al occurs during isothermal heating below the crystallization temperature. After consolidation, no glass transition occurs upon continuous heating. XRD of consolidated disc-shape samples reveal fcc-Al crystals within the residual amorphous matrix. The amount of fcc-Al crystals increases with plastic shear deformation along the disc radius and with rotation angle. The results indicate that the primary precipitation of fcc-Al is strain-induced and possibly athermal.

Keywords: amorphous aluminium alloys, metallic glass, crystallization, atomization, high

pressure torsion

1. Introduction

Aluminum-rich metallic glasses have attracted much interest due to their potential to develop nanostructured materials, which can have two to three times larger tensile strength in comparison to conventional polycrystalline Al-alloys. An increase in fracture tensile strength from 735 to 1010 MPa has been observed in Al-Fe-Gd melt-spun ribbons after partial devitrification [1]. Here, a precipitation hardening effect occurs due to a high number density of Al-nanocrystals ranging from 10^{21} to 10^{23} m^{-3} in the amorphous matrix [1,2]. The nanocrystals can be produced either by heat treatment [3] or by plastic deformation [4–9]. Deformation-induced crystallization at ambient and subambient temperatures has been observed after cold rolling [4], nanoindentation [5], high pressure torsion (HPT) [6,7] and extreme bending [8,9]. It is yet unclear whether the underlying mechanism for strain-induced crystallization is thermal or athermal.

Since Al-rich metallic glasses are marginal glassformers, they can only be synthesized by melt spinning, gas atomization, ball milling, etc. These glasses exist therefore only in limited sample dimensions such as powders, flakes or ribbons, which require consolidation to a bulk material for any structural application. As shown in few examples in the literature, consolidation by hot pressing [10] and hot extrusion [11] has to be performed at rather high temperatures (around the crystallization onset and higher) to obtain sufficiently compacted samples with low porosity. As a consequence of the high processing temperature, the bulk materials consolidated in one of these ways are usually completely crystallized and brittle. Spark sintering can be successfully performed at lower temperatures [12,13], but only temperatures above the crystallization onset yield samples with low porosity. As an alternative method, high pressure torsion (HPT) has shown consolidation at room temperature for several

alloys [6,14,15]. HPT permits consolidation of centimeter-size specimen as presented in ref. [16] for Al-Mg-Sc alloy and it is a method, which allows investigation of properties as a function of the plastic shear deformation level.

In this work, $\text{Al}_{85}\text{Ni}_{10}\text{La}_5$ alloy was chosen due to its good glass forming ability (GFA) compared to other known Al-rich metallic glasses. Gas-atomized amorphous $\text{Al}_{85}\text{Ni}_{10}\text{La}_5$ powder was subjected to HPT at room temperature in order to investigate as to which extend plastic shear straining is required to consolidate amorphous powders and if powder consolidation can lead to bulk amorphous material.

2. Experimental procedures

The master alloy with nominal composition $\text{Al}_{85}\text{Ni}_{10}\text{La}_5$ (at.-%) was synthesized in an inductively heated furnace under argon atmosphere using pure elements Al (99.98%), Ni (99.7%) and La (99.7%). The melt was heated up to approximately 1200°C and was subsequently helium gas atomized using the Nanoval process [17]. After atomization the powder was stored in air under ambient temperatures and humidity before further treatment. The consolidation of as-atomized powder was performed by HPT at room temperature using Bridgeman-type anvils, an uni-axial pressure of 6 GPa, and an angular speed of the rotating anvil of 0.3 min^{-1} . Four disc-shape samples were prepared using different rotation angles of 5°, 15°, 45° and 360° for the upper anvil. In the following, these discs are denoted as D5, D15, D45 and D360. The samples have a diameter of 8 mm and a thickness between 90 and 180 μm . All of them were brittle and broke into 2 or more pieces.

Inductively coupled plasma mass spectroscopy (ICP-MS) measurements on as-atomized powders were performed to check the relative chemical composition of the alloy after atomization. Three replicates of approximately 10 mg per sample were prepared by

dissolving the powder in highly concentrated HNO₃ (400 µl) under stepwise heating from 60 to 90°C and continuous shaking. Data analysis was done assuming that only Al, Ni and La are present in the sample material. The intensities of Al and Ni with respect to La were determined and a mean value was calculated from 30 measurements per sample. The comparison of relative intensities of the sample with that of the standard solution yielded the stoichiometric concentration of the sample. The results presented here are the calculated mean of three replicates per sample. The estimated error is approximately 0.1 at.-%. Further details about the analyzing method are given in ref. [18].

Scanning electron microscopy (SEM) on powders and disc samples was done using a Philips XL30 ESEM and a Zeiss CrossBeam 1540ESB, which were operated between 5 and 20 keV. The powder particle size distribution was measured with a CILAS 715 granulometer.

Angle-dispersive (AD) XRD measurements on mechanically and thermally treated specimens were carried out by means of a Bruker D8 Advance diffractometer using Cu-K α radiation (wavelength $\lambda = 0.154$ nm). The X-ray illuminated area was circular with a diameter of 6 mm. AD XRD experiments during heating were done in-situ at the magnetic bending beam line KMC-2 at the Berlin synchrotron radiation facility BESSY using a monochromatic X-ray beam of 8 keV photon energy ($\lambda = 0.154$ nm). Powder samples were poured on a ceramic sample holder and measured in reflection mode. D360 sample parts were fixed on a Cu sample holder and measured in transmission mode. The sample holder was mounted on a resistance heater situated on a goniometer inside an evacuated high temperature chamber. The chamber was equipped with a beryllium dome, which is almost transparent for the photons used. Diffracted X-rays were acquired by means of a 2D-detector. Samples were subjected to constant heating at 10 K/min, while XRD patterns were acquired every 5 s corresponding to a temperature change of approximately 0.9 K. Temperature control was realized by two

thermocouples placed on the sample holder and the resistance heater, respectively. The recorded diffraction data in form of Debye-Scherrer ring parts were integrated in order to achieve XRD intensity profiles. Diffuse scattering by the beryllium dome and the time-dependent intensity decay of the incident beam was considered and subtracted. Corundum powder was used to calibrate the positions of the Bragg reflections. Alloy phases were identified by the search and match method using PDF-2-data of the International Center for Diffraction Data [19]. The average crystallite size was calculated from full-width-at-half-maximum (FWHM) of fitted peaks by use of Scherrer's formula. The volume fraction of deformation-induced fcc-Al phase in disc D360 was roughly calculated from XRD patterns of disc D360 by dividing peak areas of fcc-Al Bragg reflections with the scattering intensity of the amorphous phase.

Energy-dispersive (ED) XRD measurements on a D360 sample piece were performed at the EDDI-beamline at the 7 T multipole wiggler of BESSY [20]. An intense white X-ray beam was used to record the diffraction patterns in transmission mode by an ED detector situated at $2\Theta = 7^\circ$. The illuminated area per measurement was $0.5 \times 0.5 \text{ mm}^2$. The primary beam was filtered by means of Al-pieces in order to prevent sample heating by low energy X-rays [21]. After each measurement the disc was translated along the radius in steps of 0.5 mm. The acquisition time per measurement was 1 hour. ED XRD patterns were analyzed as follows: The broad diffuse scattering of the amorphous phase was fitted by means of a linear function in the vicinity of the Bragg peak and subtracted. The peak area of the Bragg reflections was obtained from a fit using a Gaussian function. The fit is background corrected in order to take into account variations of the specimen thickness. The identification of Al Bragg peaks was done by determining the Bragg peak positions from its lattice parameters using kinematic diffraction theory.

Continuous and isothermal differential scanning calorimetry (DSC) experiments were carried out under a stream of argon gas using a Perkin-Elmer DSC Pyris 1. After the first run of the amorphous sample, a second run under the same conditions on the fully crystallized sample was performed to determine the baseline which was subtracted from first-run data. Kissinger analysis was applied in order to determine activation energies of phase transformations in as-atomized powders. The procedure used is described in [22, 23]. The analysis required DSC data from continuous heating experiments performed at different heating rates ranging from 2.5 to 80 K/min. Additionally differential thermal analysis (DTA) measurements on amorphous powder were performed under a stream of argon gas using a Netzsch DTA 404C.

3. Results and discussion

3.1 Powder characterization

ICP-MS analysis of the as-atomized $\text{Al}_{85}\text{Ni}_{10}\text{La}_5$ powders used in our experiments confirms approximately its nominal chemical composition (85.3 at.-% Al, 9.7 at.-% Ni, and 5.0 at.-% La). As-atomized powder particles have a spherical shape and a smooth surface, see figure 1(a). Hot welded particle satellites were rarely detected. Individual dendrites of approximately 1 to 2 μm size are observed on the surface of powder particles with particle diameter $d \geq 25 \mu\text{m}$, see figure 1(b). The presence of dendrites is ascribed to the lower cooling rate in large particles. Because as-atomized powders appear to be amorphous in the XRD experiment (figure 2), the dendrite volume fraction is regarded to be rather low ($< 5\%$) in comparison to the amorphous phase. Granulometry yields an uni-modal powder particle distribution with a most frequent particle diameter $d = 6 \mu\text{m}$, see figure 3. The cumulative particle size distribution yields a mean particle diameter $d = 11 \mu\text{m}$. This result takes into

account powder particles with diameter $d > 2 \mu\text{m}$. Particles with $d < 2 \mu\text{m}$ cannot be detected by granulometry. It is noteworthy, that helium-atomization of $\text{Al}_{85}\text{Ni}_{10}\text{La}_5$ alloy by means of the Nanoval process permits to achieve largely amorphous powders in one processing step without further sieving. This is mainly due to a large relative amount of small powder particles.

The thermal stability of the amorphous powder was studied by means of DSC and XRD in order to determine maximum temperatures and maximum dwelling times, at which consolidation experiments could be performed without crystallization. The baseline-subtracted DSC signal of amorphous powder measured upon continuous heating at 40 K/min is presented in figure 4(a). A small exothermic heat release occurs between 125 and 250°C, see figure 4(b). This dissipation of heat can be assigned to structural relaxation of the amorphous phase. An exothermic reaction prior to glass transition has also been observed in amorphous melt-spun ribbons of $\text{Al}_{88}\text{Y}_7\text{Fe}_5$ [6] and $\text{Al}_{85}\text{Ni}_5\text{Y}_6\text{Co}_2\text{Fe}_2$ alloy [24]. These exothermic reactions were ascribed by these authors to structural relaxation within the amorphous phase. At an onset temperature of $T_g = 258^\circ\text{C}$ (figure 4(b)) an endothermic heat release develops that indicates glass transition. During further heating, a large and narrow exothermic peak occurs at an onset temperature $T_x = 277^\circ\text{C}$ (figure 4(a)) indicating the onset of crystallization. Further exothermic heat releases appear at higher temperatures, see discussion below.

The structural changes attributed to the exothermic DSC signals were investigated by AD XRD. After heating the powder specimens with a heating rate of 40 K/min up to the temperatures marked by arrows in figure 4(a). The XRD patterns in figure 4(c) show that three equilibrium phases, fcc-Al, Al_3Ni and $\text{Al}_{11}\text{La}_3$, occur after heating to temperatures above 280°C. The peak widths in XRD patterns of annealed powders decrease with annealing

temperature. Figure 4(d) illustrates the crystal growth of each phase after heating. In the temperature range from 280°C to 341°C the changes in average crystallite size of all three phases are small compared to the temperature range between 341°C and 440°C. The large crystal growth between 341°C and 440°C is reflected by the excess heat flow peak at 341°C in the DSC curve, see figure 4(a). The average crystallite size of Al₃Ni appears to decrease from 280 to 312°C. This behavior is unlikely pointing to a variance among the different annealed powder samples used. However, the average crystallite size of Al₃Ni doubles from 280 to 341°C, while that of fcc-Al increases by about 50%. Crystallites of Al₁₁La₃ hardly grow in this temperature range. Thus, the peak at 341°C in the DSC curve is mainly ascribed to crystal growth of the three phases at expense of the residual amorphous matrix.

Continuous heating DSC experiments on amorphous powders using heating rates ranging from 2.5 to 80 K/min show qualitatively similar curves with two excess heat flow peaks. The peaks shift towards higher temperatures with increasing heating rate. This is due to the reduced time for the system to respond to faster heating. (Kissinger analysis using the first peak associated to the crystallization start for each heating rate yields an activation energy of 292 kJ/mol.) Based on this observation we conjecture that structural changes attributed to these exothermic reactions are similar during heating at heating rates ranging from 2.5 to 80 K/min.

Additional information about the crystallization sequence was gained by performing an in-situ XRD experiment during continuous heating with a heating rate of 10 K/min. This heating rate was required in order to achieve a reasonable temperature resolution during heating, in which one XRD spectrum was measured. Figure 5(a) shows the temperature vs. 2-theta XRD diagram recorded during heating. Red colour indicates high intensity, while blue colour indicates low intensity. A broad diffuse scattering maximum with low intensity can be

observed during continuous heating from room temperature to 271°C. At 271°C, Bragg reflections of fcc-Al, Al₃Ni and Al₁₁La₃ develop within a small temperature range of 3 K. This sudden phase transformation is associated with the first large exothermic heat release shown in figure 5(b), that was obtained using the same heating rate of 10 K/min. Within the experimental time resolution, fcc-Al, Al₃Ni and Al₁₁La₃ crystallize simultaneously during continuous heating.

An isothermal heating DSC experiment on amorphous powder was performed at 246°C, see figure 6(a). This temperature is below the onsets of crystallization observed during continuous heating with rates between 2.5 and 80 K/min. The DSC curve shows a first exothermic heat release within 5 min of isothermal heating and a maximum exothermic heat flow after about 20 min. The first exothermic heat release is not a device transient as shown by the flat baseline within the same time range and thus, it is due to reactions in the sample. The structural changes associated with the DSC-signals were investigated by means of ex-situ XRD on powders isothermally heated at 246°C for different times. The dwelling times are marked by arrows in figure 6(a). The XRD pattern of a powder sample annealed for 5 min remain essentially unchanged compared to that of the as-atomized powder, see figure 6(b). Powder samples annealed for 10 min and 15 min show broad diffuse scattering superimposed by fcc-Al Bragg reflections with marginal intensities indicating primary crystallization of fcc-Al. After annealing a powder sample for 20 min, XRD reveals additional Bragg reflections which can be assigned to the intermetallic phases Al₃Ni and Al₁₁La₃. The Bragg reflections of Al₃Ni and Al₁₁La₃ appear in the same time period as the second broad exothermic heat flow maximum, see figure 6(a). The peak areas of the Bragg reflections increase while the peak widths decrease with annealing time indicating crystal growth of all three phases.

Since as-atomized $\text{Al}_{85}\text{Ni}_{10}\text{La}_5$ powders and powders annealed isothermally at 246°C for 5 min appear amorphous in XRD, the observed first heat release in figure 6(a) can be interpreted in terms of structural relaxation [24] and/or growth of crystals or quenched-in nuclei [23]. Yang and co-workers [24] observed that isothermal heating of amorphous $\text{Al}_{85}\text{Ni}_5\text{Y}_6\text{Co}_2\text{Fe}_2$ melt-spun ribbons show no longer monotonically decreasing exothermic heat flow after annealing up to temperatures below the onset temperature of crystallization. Since the annealed $\text{Al}_{85}\text{Ni}_5\text{Y}_6\text{Co}_2\text{Fe}_2$ ribbons were still TEM and X-ray amorphous, the DSC signal was regarded as excess heat from structural relaxation. However, this monotonically decreasing exothermic DSC signal can be also interpreted in terms of crystal growth [23]. This has been shown by Chen and Spaepen by performing DSC experiments on partially quasi-crystalline Al-Mn thin films [23]. They fitted DSC signals using Johnson-Mehl-Avrami kinetics in order to distinguish between nucleation-and-growth and growth only. As a growth signal is monotonically decreasing, the DSC signal of nucleation-and-growth is characterized by maximum exothermic heat flow similar to that shown in figure 6(a) after about 20 min of isothermal heating at 246°C . This suggests for the present Al metallic glass that a part of the excess heat at short annealing times is due to a marginal growth of dendrites detected on as-quenched powder surfaces (figure 1(b)). We believe that this heat flow is mainly due to the growth of a high number density of nuclei, which were quenched-in during the atomization process rather than due to the growth of dendrites on the surface of as-quenched powder particles. This interpretation is in agreement with the results of Zhang and coworkers [25] who studied the stability of $\text{Al}_{85}\text{Ni}_{10}\text{La}_5$ powder by means of DSC during isothermal annealing at 235°C . They found a monotonically decreasing DSC signal which they ascribed to the presence of quenched-in Al-nuclei. Indications for quenched-in nuclei in our alloy are given in the X-ray diffractogram of as-atomized powders, see figure 6(b). Here, the diffuse

scattering in XRD patterns shows a maximum intensity at $2\Theta \approx 37^\circ$ accompanied by a faint shoulder at $2\Theta \approx 44^\circ$. These values are close to values of the (111) and (200) Bragg reflections of crystalline Al ($2\Theta = 38.5^\circ$ and $2\Theta = 44.7^\circ$, respectively). The shoulder at $2\Theta \approx 44^\circ$ suggests the presence of crystalline Al clusters within the amorphous phase. This interpretation in terms of Al-rich clusters is supported by 3-DAP measurements performed on (as-quenched) melt-spun $\text{Al}_{89}\text{Ni}_6\text{La}_5$ [27] and melt-spun $\text{Al}_{88}\text{Ni}_{5.2}\text{Yb}_{6.8}$ ribbons [28]. In addition, the prepeak at $2\Theta \approx 20^\circ$ within the diffuse scattering intensity can be ascribed to medium-range order in the residual amorphous phase, as shown e.g. in XRD and X-ray absorption fine structure measurements on amorphous $\text{Al}_{89}\text{La}_6\text{Ni}_5$ melt-spun ribbons [26]. According to Saksl et al. [26], a small number of Ni-La, La-La contact pairs may contribute to the prepeak in the XRD patterns of amorphous $\text{Al}_{89}\text{La}_6\text{Ni}_5$ melt-spun ribbons.

According to the crystallization scenario in Al-rich glasses given by Perepezko [2], Al crystallizes first by rejection of solute atoms into the residual amorphous matrix. During further growth of Al crystals the amorphous matrix enriches with solute atoms in the vicinity of Al crystals until the concentration of intermetallic phases is reached. The residual amorphous phase then transforms polymorphously into the corresponding intermetallic phases. Al-Ni-La alloys with a content of alloying elements below 15 at-% ($\text{Ni} \leq 8$ at-%) show either a two or three stage crystallization sequence during continuous heating [29–31]. Sahoo et al. [29, 30] reported that primary crystallization of these glasses is either attributed to the formation of fcc-Al or to the formation of fcc-Al and a metastable phase with bcc crystal structure. They observed that the higher the content of alloying elements, the higher the temperature for primary crystallization. Furthermore, the results of Sahoo et al. and Ronto et al. show that a metastable phase occurs in Al-rich Al-Ni-La alloys if the La content exceeds 5 at.-% [29–31]. A metastable crystalline Al_3La phase along with Al, Al_3Ni and $\text{Al}_{11}\text{La}_3$ was

found by Zhang and coworkers [25] after heating of helium-atomized $\text{Al}_{85}\text{Ni}_{10}\text{La}_5$ powder to 263 °C with a constant heating rate of 10K/min and a hold time of 5 min at 263°C. This is contrary to our observations where no metastable phase was detected upon annealing. The reasons for this discrepancy might lie in the different parameters used for the heat treatment in our work and in the work of Zhang. It is known, that the phases which form during heat treatment depend sensitively on the parameters used for the heat treatment [25].

As a consequence of the results described above, consolidation of amorphous $\text{Al}_{85}\text{Ni}_{10}\text{La}_5$ powders should be completed within a processing time $t \leq 10$ min at $T \leq 246^\circ\text{C}$ if the amorphous phase is to be retained. Since these temperatures are too small to cause powder particle bonding by sintering ($T_{\text{sintering}} \approx (2/3) T_m$ [32], with $T_m = 803\text{--}1073$ K, equivalent to 630–800°C, as measured on as-atomized $\text{Al}_{85}\text{Ni}_{10}\text{La}_5$ powders by means of DTA at 10 K/min) or hot welding during consolidation processing, HPT is one approach for low temperature consolidation of amorphous Al-alloy powders by means of severe plastic shear deformation.

3.2 Samples produced by high pressure torsion

SEM-images in figure 7(a) show the radial, cross-sectional fracture surface of disc D360. They reveal a three layer sandwich structure. Top and bottom layers increase in thickness along the radius from the disc center to the disc edge, while the total disc thickness decreases. The middle layer exhibits powder particles, see figures 7(b) and 8, that are well integrated and slightly elongated in radial direction reflecting the direction of the applied forces. An enlarged area of the top layer in figure 7(c) shows vein patterns. Considering vein patterns as being characteristic for fracture surfaces of bulk metallic glasses [33], the present vein pattern containing layers can be regarded as fully consolidated while being still

amorphous. In this context, consolidation means that the powder particles are merged, probably by cold-welding, because no powder features occur. Consequently, this observation points to an increasing consolidation/ densification of powders with increasing plastic shear deformation along the disc radius. Different relationships can be used to estimate strain values [14]. An equivalent strain ϵ_{eq} can be calculated according to [34]:

$$\epsilon_{eq} = \ln((1 + \gamma^2)^{1/2}) \quad (1)$$

with the shear strain $\gamma = \theta R/L = 2\pi NR/L$, where θ , N , R and L denote the rotation angle in radians, number of rotations, disc radius and disc thickness, respectively. The evolution of ϵ_{eq} along the disc radius according to equation 1 for all samples is displayed in figure 9. It shows that the plastic shear deformation increases drastically along R for $R \leq 1\text{mm}$ if the rotation angle is large (D360). For values $R > 1\text{mm}$ (D360), the plastic shear deformation increases slightly with increasing R compared to $R \leq 1\text{ mm}$.

The observed sandwich structure indicates that the degree of consolidation is higher towards the powder-anvil interfaces, probably due to an increasing plastic shear deformation in normal direction relative to half thickness. In addition, the fracture surface of disc D360 reveals vein patterns also in the center ($R = 0$) of the upper and lower layer indicating that consolidation occurs also in regions where plastic shear deformation is zero according to eq. 1. Obviously, equation 1 cannot explain the observed sandwich structure, but a critical strain level can be estimated at which the powder particles start to merge. Since no vein patterns were detected throughout the whole radial fracture surface in sample D45, the equivalent strain ϵ_{eq} necessary to merge powder particles has to be larger than 3, see figure 9. Consolidation in the disc center may originate from shear strain associated to the reduction of disc thickness by material-flow during HPT processing [6]. According to Boucharat et al. [6], the shear strain ϵ_{eq} attributed to material-flow in the center ($R = 0$) is about 0.7, which is too

small for powder consolidation. Therefore material-flow alone cannot be the only reason for consolidation in the center region. Moreover, our results show that higher deformation levels are required to achieve full consolidation. It was reported that 5 turns of the anvils yield fully (merged powders) consolidated discs of $\text{Al}_{88}\text{Y}_7\text{Fe}_5$ alloy [6] and $\text{Al}_{90}\text{Fe}_7\text{Zr}_3$ alloy [15].

XRD measurements on samples after HPT were performed in order to clarify, if the structure has changed compared to the as-atomized state. Figure 10(a) shows energy-dispersive XRD patterns of disc D360 that were measured in steps of 0.5 mm along the disc radius. XRD patterns at the disc center show a broad diffuse scattering maximum similar to XRD patterns of as-atomized powder, whereas the XRD patterns at the disc edge exhibit a broad diffuse scattering maximum superimposed by (111) and (200) fcc-Al Bragg reflections. The peak areas of (111) and (200) fcc-Al Bragg reflections increase with radius from 0 to 3.5 mm, see figure 10(b). Hence, the volume-fraction of fcc-Al phase increases with plastic shear deformation indicating that the crystallization of fcc-Al is deformation-induced. Al crystals also occur in the disc center (figure 10(b)), though no shear strain is induced there according to Eq. 1 (see figure 9). The presence of Al crystals in the disc center could originate either from a strain of the order of 0.7 associated to the reduction of the disc thickness [6] or from a high uni-axial pressure [35]. Whether fcc-Al crystals are exclusively located in the top and bottom layers or not, cannot be derived from ED XRD data, because the measurements were done in transmission mode. Since disc D45 also shows fcc-Al crystals in a residual amorphous matrix, see figure 11, deformation-induced crystallization of fcc-Al occurs also in regions where the cross-sectional fracture surface still shows powder particles in the entire range. Moreover, plastic deformation and friction during HPT processing cause the sample temperature to increase. During HPT processing at room temperature the sample temperature is estimated to be far below 100°C [14]. This temperature increase is far below the

crystallization temperature of amorphous $\text{Al}_{85}\text{Ni}_{10}\text{La}_5$ powders. The temperature increase is negligible due to the relatively small strain rate and good thermal conductivity between small sample and large anvils.

Besides different deformation levels along the disc radius, an influence of the anvil rotation angle upon deformation-induced crystallization of fcc-Al was observed. Figure 11 shows a broad diffuse scattering maximum and fcc-Al Bragg reflections in AD XRD patterns of discs D45 and D360. The volume fraction of deformation-induced fcc-Al phase in disc D360 is about 3%. The Cu Bragg reflection visible in specimen D5 is caused by Cu powder contaminations of a precedent HPT experiment. D5 and D15 do not show fcc-Al Bragg reflections indicating that $\epsilon_{\text{eq}} > 2$ is necessary to induce a sufficiently large volume fraction of fcc-Al phase detectable for AD XRD. Moreover, deformation from uni-axial pressure and flow alone does not yield enough fcc-Al phase detectable for AD XRD experiments, because fcc-Al Bragg reflections do not occur in D5 and D15. Top and bottom side of each disc reveal similar XRD patterns (not presented here) indicating the same structure in top and bottom layer.

The present HPT experiments on amorphous $\text{Al}_{85}\text{Ni}_{10}\text{La}_5$ powders show a correlation between deformation level and amount of fcc-Al phase precipitated within the residual amorphous matrix, see figure 10 and figure 11. Heating experiments on amorphous $\text{Al}_{85}\text{Ni}_{10}\text{La}_5$ powder revealed that intermetallic phases occur almost simultaneously with fcc-Al, see figure 5. If a local temperature spike -e.g. in shear bands- during plastic deformation induced crystallization, then the formation of intermetallic phases would be expected. The fact that only fcc-Al crystals and no intermetallic phases precipitate upon plastic deformation, points to an athermal crystallization mechanism [6–8, 36–38].

Further evidence that intermetallic phases were not formed during HPT is given by

in-situ XRD measurements performed at both the center and the edge regions of disc D360 during continuous heating with a rate of 10 K/min, see figure 12. At room temperature, XRD patterns of the edge region of disc D360 exhibit visibly fcc-Al Bragg reflections whereas the center region of disc D360 exhibits only vague indications of fcc-Al Bragg reflections. This difference in intensity of fcc-Al Bragg reflections between the center and the edge region is in qualitative agreement with ED XRD measurements shown in figure 10(a).

The intensity of fcc-Al Bragg reflections increases during continuous heating from room temperature to 274°C and 291°C in the center and edge region of D360, respectively, indicating an increase in volume amount of fcc-Al phase. Bragg reflections indicating intermetallic phases are not present in the diffraction patterns. If intermetallic phases were present in plastically deformed powders, they would be expected to grow during continuous heating at 10 K/min. At 274°C and 291°C the diffuse scattering signal of the amorphous phase disappears, and Bragg reflections of fcc-Al, Al₃Ni and Al₁₁La₃ develop within a narrow temperature range of about 3 K. At further heating up to 400°C, all Bragg peaks move to smaller 2 Θ -values due to the thermal expansion of the crystal lattice.

Figure 13(a) shows baseline-corrected DSC signals of samples extracted from the edge and center region of disc D360 and from the edge region of discs D5, D15 and D45 obtained during continuous heating at 40 K/min. Compared to as-atomized powder, the peak area of the exothermic heat flow at about 277°C corresponding to the crystallization of fcc-Al, Al₃Ni, and Al₁₁La₃ decreases with increasing plastic deformation (radius, torsion angle). At the same time the peak area of exothermic events between 290 and 350°C increases with increasing torsion angle, see figure 13(a). The total heat release over all exothermic events decreases from 120 J/g of D5 edge, 116 J/g of D15 edge, 98 J/g of D45 edge to 93 J/g of D360 edge. This is in qualitative agreement with an increasing volume fraction of

deformation-induced fcc-Al indicated by an increasing peak area of fcc-Al Bragg reflections in figures 10 and 11 indicating an increasing volume fraction of deformation-induced fcc-Al. Moreover, the decreasing exothermic heat flow from the D360 center to the edge at about 277°C in figure 13(a) corresponds to the shift of temperatures of the complete crystallization, see figure 12. This indicates that in the temperature range between 277 and 290°C intermetallic phases are not detectable by means of XRD in D360 edge specimen. The volume amount of intermetallic phases is therefore supposed to be smaller than that of as-atomized powders and D360 center.

Though XRD measurements on HPT-consolidated samples show that a large amount of residual amorphous phase is still present, a glass transition was not observed in the DSC signal of HPT-consolidated samples upon continuous heating, see figure 13(b). This points at a “fragile”-“strong glass” transition of the amorphous phase as it also was observed by Louzguine et al. [39] by variation of the Sc content in $\text{Al}_{84}\text{Y}_9\text{Ni}_5\text{Co}_2$ alloy.

Adequate heat treatment of amorphous $\text{Al}_{85}\text{Ni}_{10}\text{La}_5$ powder results in nanocrystalline structures (crystal size $> 18 \pm 4$ nm) pointing at a nucleation-controlled crystallization process [2]. Since HPT performed at room temperature to sufficiently large torsion angles $\geq 45^\circ$ induces a high number density of nanocrystals (D360: crystallite size $\approx 7 \pm 2$ nm, and a volume fraction of about 3%, corresponding to a number density of $\approx 2 \times 10^{23} \text{ m}^{-3}$), deformation-induced crystallization can be discussed in the light of classical nucleation theory. According to Christian [41], the nucleation rate I for homogeneous nucleation can be written as

$$I = C \exp(-\Delta G_c/k_B T) \exp(-\xi/k_B T) \quad (2)$$

where ΔG_c is the energy required to form a nucleus of critical size, ξ is the activation energy for diffusion of a matrix atom to the nucleus, k_B is Boltzmann’s constant, T is the temperature,

and C is a constant. As recently stated by Lee et al. [35], ΔG_c and ξ are reduced with increasing uni-axial pressure during plastic deformation of a Cu-based metallic glass. ΔG_c is reduced by one order of magnitude when the uni-axial pressure is increased from 0.2 to 2 GPa, and by a factor of 25 if the pressure goes up to 5 GPa [35]. In comparison, ξ decreases only by about 20% with increasing uni-axial pressure from 0.2 to 5 GPa. Hence, we ascribe deformation-induced crystallization of fcc-Al in amorphous $\text{Al}_{85}\text{Ni}_{10}\text{La}_5$ powders to a tremendous decrease in ΔG_c and a significant decrease in ξ in analogy to the interpretation of deformation-induced crystallization of a Cu-based metallic glass by Lee and co-workers [35]. During plastic shear deformation by means of HPT, ΔG_c decreases because the system is steadily driven away from local metastable equilibrium of the amorphous configuration by dynamical input of strain energy [2]. ξ decreases at the same time due to increasing free volume localized in shear bands [40, 42, 43]. A local temperature rise in shear bands, as observed by Lewandowski and Greer [44] during plastic deformation of the Zr-based bulk metallic glass Vitreloy 1, can promote nucleation of fcc-Al in amorphous $\text{Al}_{85}\text{Ni}_{10}\text{La}_5$ powders according to Eq. 2. Furthermore, the quenched-in nuclei and inhomogeneities in amorphous $\text{Al}_{85}\text{Ni}_{10}\text{La}_5$ powders may also promote crystallization because they can act as sites for stress localization and heterogeneous nucleation [35].

4. Conclusions

Amorphous $\text{Al}_{85}\text{Ni}_{10}\text{La}_5$ powder was synthesized by helium gas atomization. As-atomized amorphous powders show a glass transition and indications of quenched-in fcc-Al nuclei. Amorphous powders crystallize upon heating and upon plastic shear deformation. Isothermal and continuous heating reveal that fcc-Al, Al_3Ni , and $\text{Al}_{11}\text{La}_3$ crystallize simultaneously in a small time and temperature range. In contrast, plastic shear deformation at room temperature by HPT leads only to deformation-induced crystallization of

fcc-Al phase within the amorphous matrix. The volume fraction of deformation-induced fcc-Al nanocrystals increases with plastic shear deformation. This observation is explained by classical nucleation theory, because plastic deformation can reduce the activation energy for crystallization at a given temperature. The absence of intermetallic phases after HPT indicates that deformation-induced crystallization of fcc-Al is not caused by a temperature spike during deformation. HPT consolidated samples show no glass transition in the DSC signal. HPT can be used to consolidate amorphous powders at room temperature. The densification level depends on the extent of plastic shear applied. The amorphous phase cannot be fully conserved during HPT processing because deformation-induced crystallization of fcc-Al cannot be avoided. However, in addition to thermal treatment, plastic shear deformation by HPT can be used as alternative strategy to tailor nanostructured Al materials.

Acknowledgements

The authors would like to thank D. Köpnick-Welzel for operating the Zeiss CrossBeam 1540ESB, C. Jimenez for performing the DTA experiment, Y. Yermakov, Ch. Abromeit, and N.P. Lazarev for setting up the cooperation with RAS Yekaterinburg.

References

- [1] H. Chen, Y. He, G.J. Shiflet, S.J. Poon, *Scripta Mater.* 25 (1991) 1421-1424.

- [2] J.H. Perepezko, *Prog. Mater. Sci.* 49 (2004) 263-284.

- [3] A.P. Tsai, T. Kamiyama, Y. Kawamura, A. Inoue, T. Masumoto, *Acta Mater.* 45 (1997) 1477-1487.

- [4] J.H. Perepezko, R.J. Hebert, R.I. Wu, *Mater. Sci. Forum* 386-388 (2002) 11-20.

- [5] J.-J. Kim, Y. Choi, S. Suresh, A.S. Argon, *Science* 295 (2002) 654-657.

- [6] N. Boucharat, R. Hebert, H. Rösner, R. Valiev, G. Wilde, *Scripta Mater.* 53 (2005) 823-827.

- [7] Zs. Kovács, P. Henits, A.P. Zhilyaev, A. Révész, *Scripta Mater.* 54 (2006) 1733-1737.

- [8] W.H. Jiang, F.E. Pinkerton, M. Atzmon, *Scripta Mater.* 48 (2003) 1195-1200.

- [9] H. Chen, Y.He, G.J. Shiflet, S.J. Poon, *Nature* 367 (1994) 541-543.

- [10] Y. Kawamura, H. Mano, A. Inoue, *Scripta Mater.* 44 (2001) 1599-1604.

- [11] A. Inoue, H. Kimura, J. Light Metals 1 (2001) 31-41.
- [12] P.P. Choi, J.S. Kim, O.T.H. Nguyen, D.H. Kwon, Y.S. Kwon, J.C. Kim, Mater. Sci. Eng. A 449-451 (2007) 1119-1122.
- [13] T. T. Sasaki, J. Vierke, M. Wollgarten, J. Banhart and K. Hono, Mater. Sci. Eng. A 490 (2008) 343-350.
- [14] R.Z. Valiev, R.K. Islamgaliev, I.V. Alexandrov, Prog. Mater. Sci. 45 (2000) 103-189.
- [15] W.J. Botta Filho, J.B. Fogagnolo, C.A.D. Rodrigues, C.S. Kiminami, C. Bolfarini, A.R. Yavari, Mater. Sci. Eng. A 375-377 (2004) 936-941.
- [16] G. Sakai, K. Nakamura, Z. Horita, T.G. Langdon, Mater. Sci. Eng. A 406 (2005) 268-273.
- [17] L. Gerking, Powder Metall. Int. 25 (1993) 59-65.
- [18] K. Heumann, S. Gallus, G. Rädlinger, J. Vogl, J. Anal. Atomic Spectrom. 13 (1998) 1001-1008.
- [19] Bruker DIFFRAC Plus software - International Center for Diffraction data
- [20] C. Genzel, I.A. Denks, J. Gibmeier, M. Klaus, G. Wagner, Nucl. Instrum. Methods A578 (2007) 23-33.

- [21] I.A. Denks, Ch. Genzel, *Mater. Sci. Forum* 571-577 (2008) 189-195.
- [22] H.E. Kissinger, *Anal. Chem.* 29 (1957) 1702-1706.
- [23] L.C. Chen, F. Spaepen, *J. Appl. Phys.* 69 (1991) 679-688.
- [24] H.W. Yang, J.Q. Wang, *Scripta Mater.* 55 (2006) 359-362.
- [25] Z. Zhang, D. Witkin, E. Lavernia, *J. Non-Cryst. Solids* 351 (2005) 1646-1652.
- [26] K. Saksl, P. Jóvári, H. Franz, Q.S. Zeng, J.F. Liu, J.Z. Jiang, *J. Phys-Condens. Mat.* 18 (2006) 7579-7592.
- [27] B. Radiguet, N. Wanderka, K.L. Sahoo, D. Blavette, J. Banhart, *Appl. Phys. Lett.* 92 (2008) 103126.
- [28] D. Isheim, D.N. Seidman, J.H. Perepezko, G.B. Olson, *Mater. Sci. Eng. A* 353 (2003) 99-104.
- [29] K.L. Sahoo, M. Wollgarten, K.B Kim, J. Banhart, *J. Mater. Res.* 20-11 (2005) 2927-2933.
- [30] K.L. Sahoo, M. Wollgarten, J. Haug, J. Banhart, *Acta Mater.* 53 (2005) 3861-3870.

- [31] V. Ronto, L. Battezzati, A.R. Yavari, M. Tonegaru, N. Lupu, G. Heunen, *Scripta Mater.* 50 (2004) 839-843.
- [32] W. Schatt, VDI-Verlag, Düsseldorf (1992).
- [33] C.A. Schuh, T.C. Hufnagel, U. Ramamurty, *Acta Mater.* 55 (2007) 4067-4109.
- [34] I. Saunders, J. Nutting, *Met. Sci.* 18 (2007) 571-575.
- [35] S.-W. Lee, M.-Y. Huh, S.-W. Chae, J.-C. Lee, *Scripta Mater.* 54 (2006) 1439-1444.
- [36] W.H. Jiang, M. Atzmon, *Acta Mater.* 51 (2003) 4095-4105.
- [37] R.J. Hebert, J.H. Perepezko, H. Rösner, G. Wilde, *Scripta Mater.* 54 (2006) 2529.
- [38] Y. Zhang, A.L. Greer, *Appl. Phys. Lett.* 89 (2006) 071907.
- [39] D.V. Louzguine, S. Sobu, A. Inoue, *Appl. Phys. Lett.* 85 (2004) 3758-3759.
- [40] F. Spaepen, *Acta Metall. Mater.* 25 (1977) 407-415.
- [41] J.W. Christian, Pergamon Press 3rd ed. (2002).
- [42] A.S. Argon, *Acta Metall. Mater.* 27 (1979) 47-58.

[43] G. Mazzone, A. Montone, M. Vittori Antisari, *Phys. Rev. Lett.* 65 (1990) 2019-2022.

[44] J.J. Lewandowski, A.L. Greer, *Nature Mater.* 5 (2006) 15-18.

Figure Captions

Figure 1: SEM images of as-atomized $\text{Al}_{85}\text{Ni}_{10}\text{La}_5$ powder showing particles smaller than 22 μm diameter (a) and one particle of about 45 μm diameter (b).

Figure 2: XRD patterns of as-atomized $\text{Al}_{85}\text{Ni}_{10}\text{La}_5$ powder.

Figure 3: Powder particle size distribution of as-atomized $\text{Al}_{85}\text{Ni}_{10}\text{La}_5$ powder.

Figure 4: (a) DSC signal of as-atomized $\text{Al}_{85}\text{Ni}_{10}\text{La}_5$ powder obtained during continuous heating at 40 K/min illustrating the tangent projections for determination of onset of T_x . (b) Enlarged area of the DSC curve shown in (a) illustrating the tangent projection for determination of the onset of T_g . (c) XRD patterns taken from powders after continuous heating at 40 K/min up to the temperatures marked by arrows in (a). (d) Crystallite sizes determined by applying Scherrer's equation to the FWHM of the XRD patterns shown in (c)

Figure 5: (a) In-situ XRD plot of as-atomized $\text{Al}_{85}\text{Ni}_{10}\text{La}_5$ powder obtained during continuous heating at 10 K/min. The intensity is expressed by different colors. Capital letter A, N and L denote Bragg reflections of fcc-Al, Al_3Ni and $\text{Al}_{11}\text{La}_3$ phase, respectively. (b) DSC curve corresponding to (a) was measured under identical conditions.

Figure 6: (a) DSC-signal of as-atomized $\text{Al}_{85}\text{Ni}_{10}\text{La}_5$ powder obtained during isothermal heating at 246°C (grey color). The DSC-signal (baseline, black color) of fully crystallized powder is painted in black and denotes the baseline. (b) XRD of as-atomized powder after

isothermal heating at 246°C and different dwelling times which are denoted by arrows in (a).

Figure 7: (a) SEM-images of the radial, cross-sectional fracture surface of disc D360 showing a sandwich structure with a top, middle and a bottom layer. (b) SEM-image of the middle layer region near the disc center. (c) SEM-image of an enlarged area of the top layer region.

Figure 8: SEM-image of the middle layer region showing elongated powder particles.

Figure 9: Calculated equivalent strain vs. disc radius of different disc shape specimens strained to different levels.

Figure 10: (a) Energy-dispersive XRD patterns along the disc radius of D360 and (b) the normalized peak areas of (111) and (200) fcc-Al Bragg reflections.

Figure 11: Angle-dispersive XRD patterns of the top surface of discs D5, D15, D45 and D360.

Figure 12: In-situ XRD plot of the center (a) and of the edge (b) region of disc D360 obtained during continuous heating at 10 K/min. The intensity is expressed by different colors. Capital letter A, N and L denote Bragg reflections of fcc-Al, Al₃Ni and Al₁₁La₃ phase, respectively.

Figure 13: (a) DSC curves of samples extracted from the edge and center region of HPT discs obtained during continuous heating at 40 K/min. (b) Enlarged area of (a) near the glass transition of as-atomized powders.

Corresponding Author

Jens Vierke

Siemens Energy

Huttenstrasse 12, 10553 Berlin, Germany

E-mail : jens.vierke@siemens.com, jensvierke@web.de

Tel : +49 30 3461 1622

Mobile : +49 176 2064 9013

Fax : +49 30 3461 2138

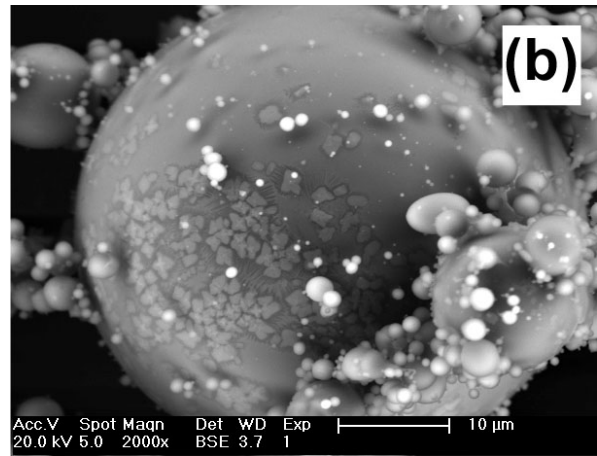
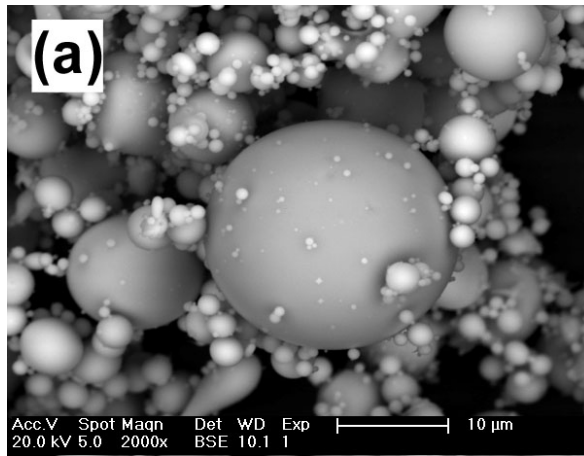


Fig. 1

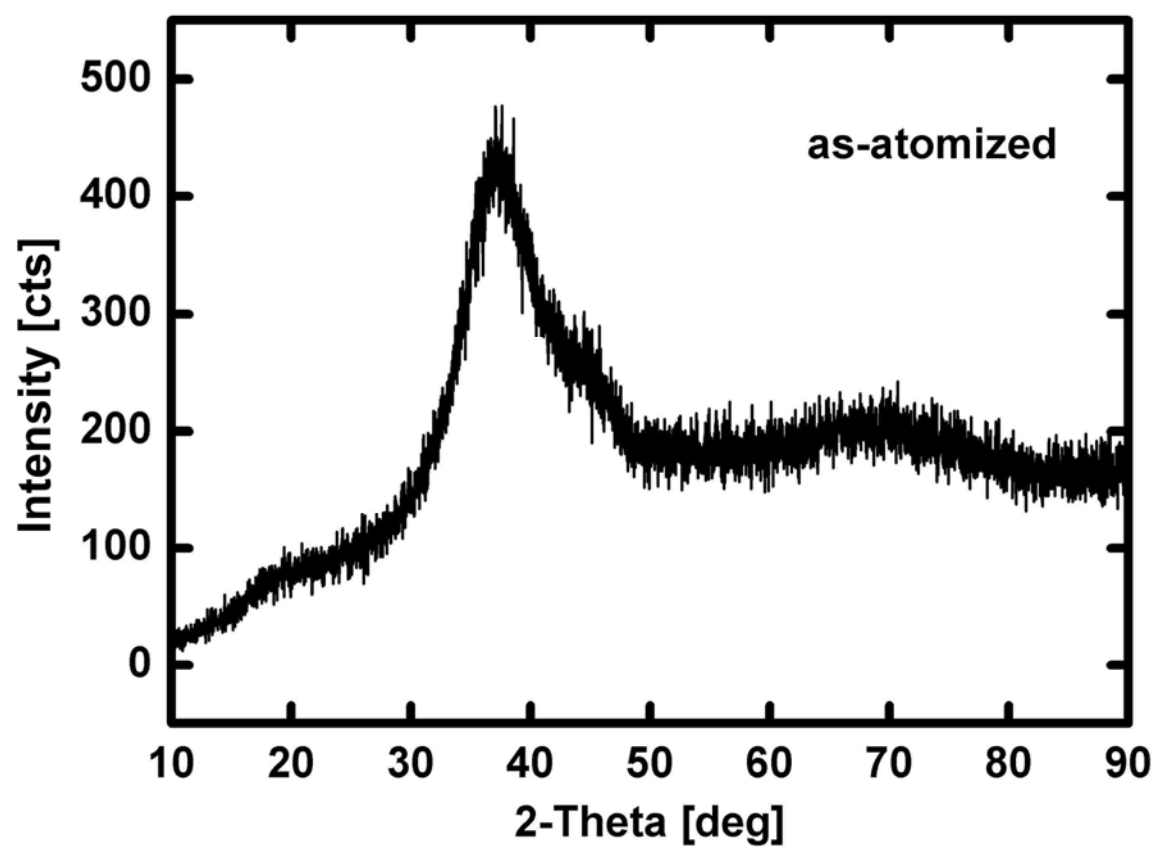


Fig.2

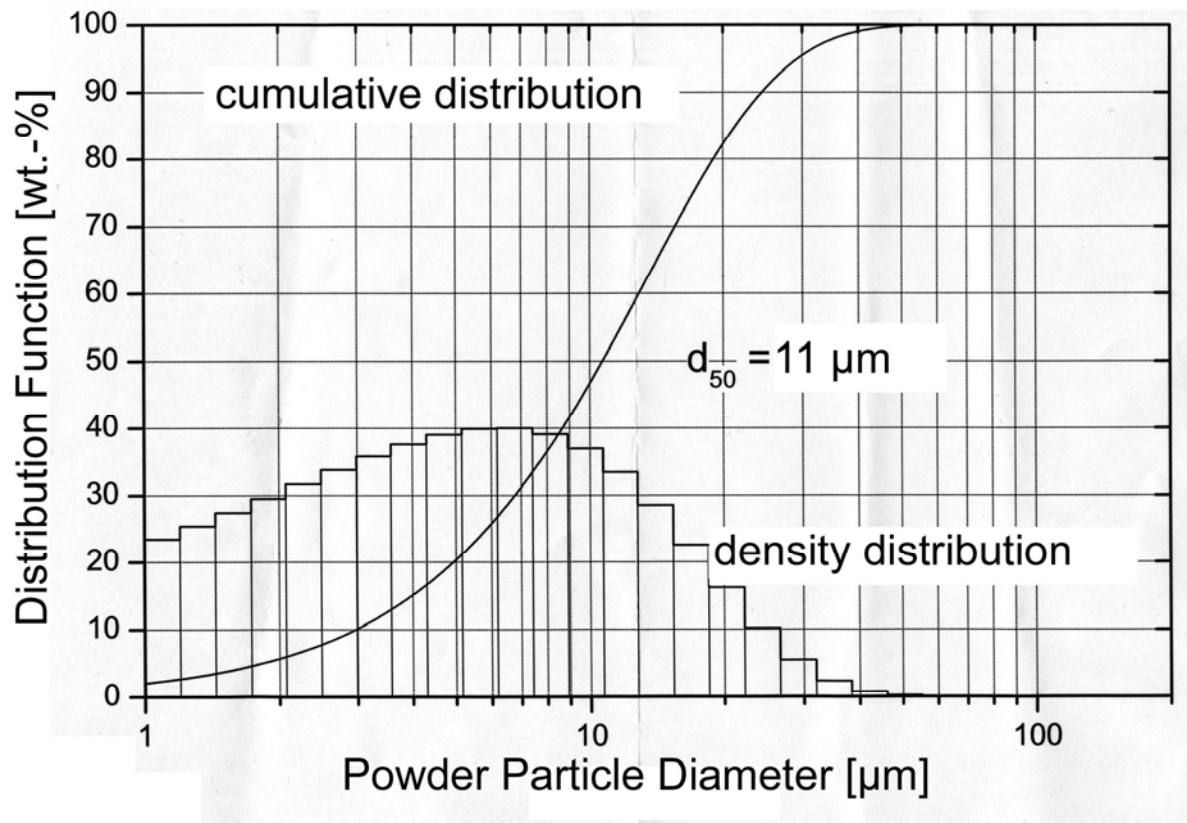


Fig. 3

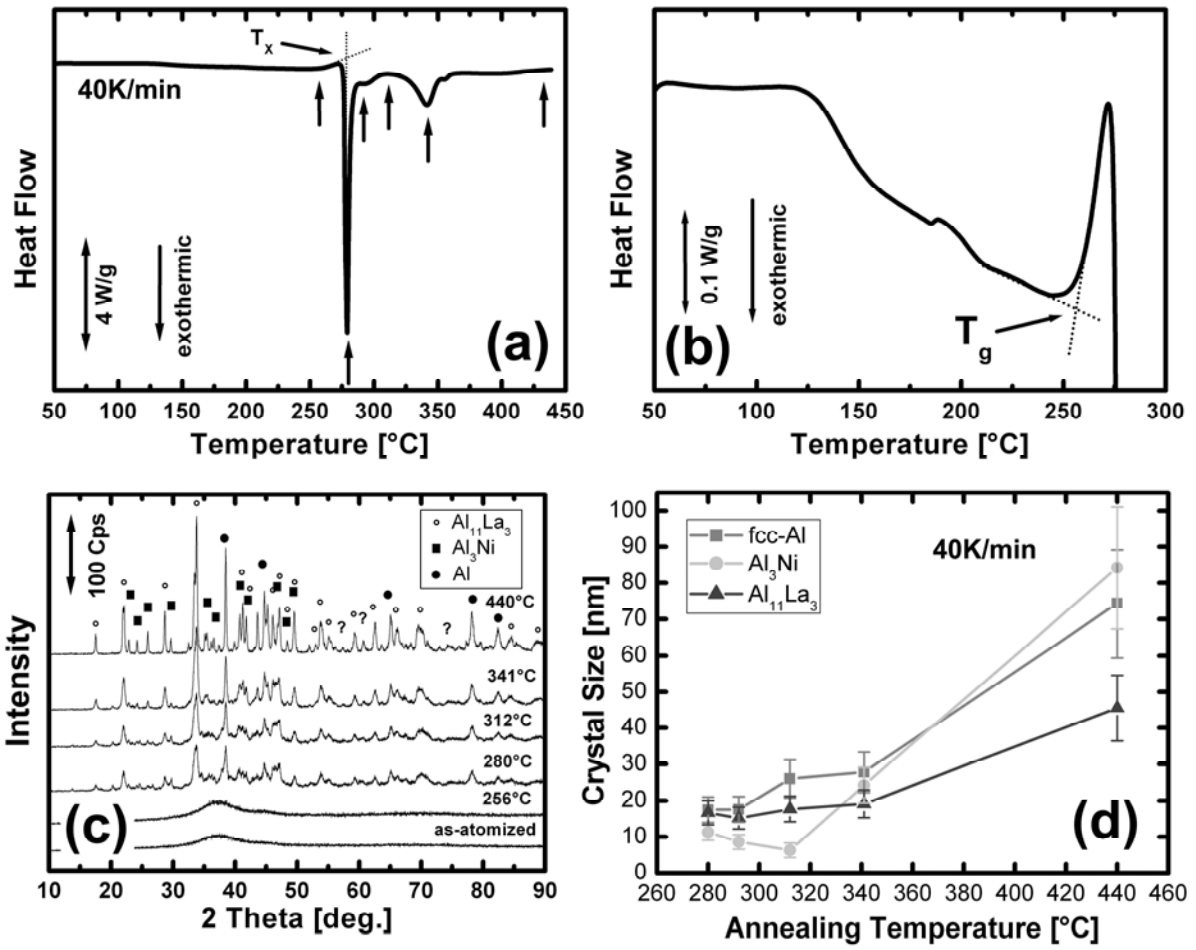


Fig. 4

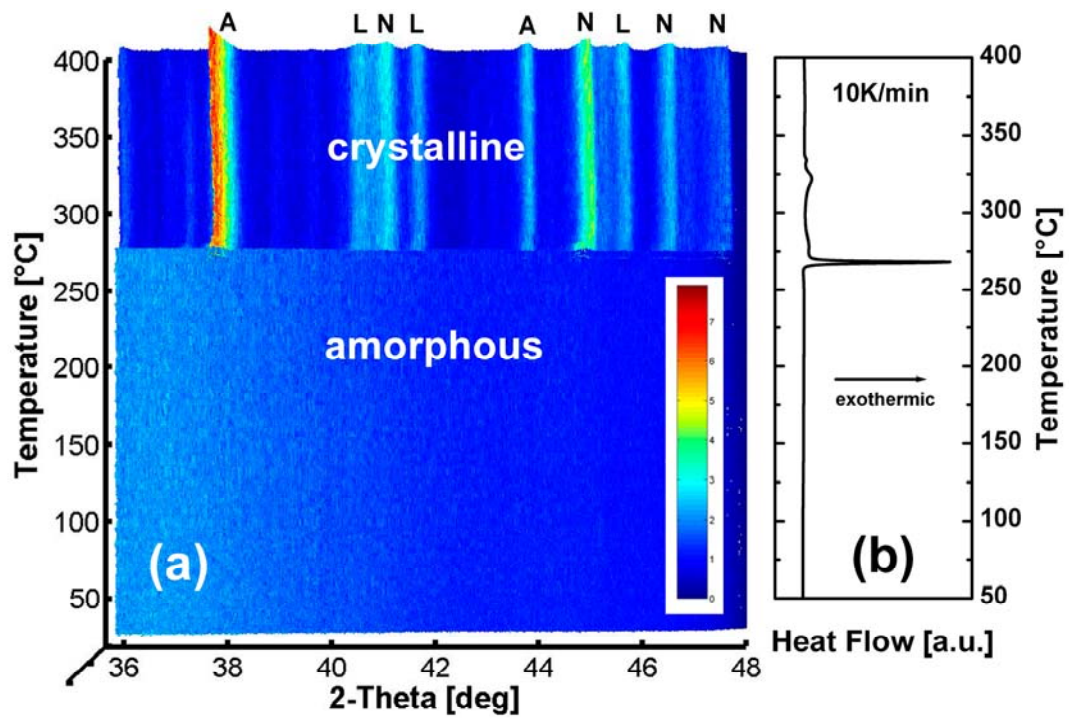


Fig. 5

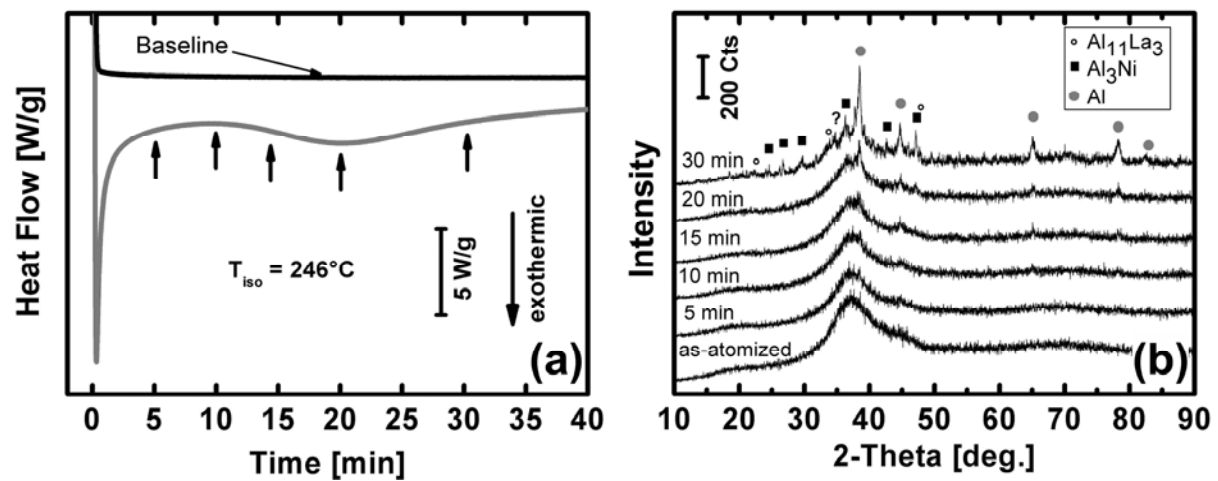


Fig. 6

Fig. 6

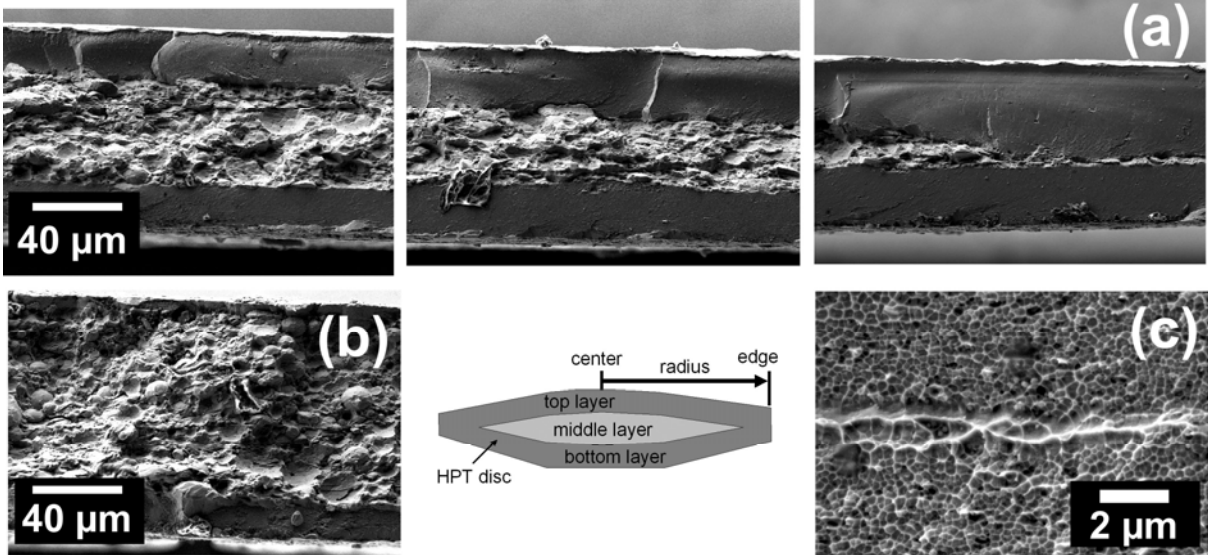


Fig. 7

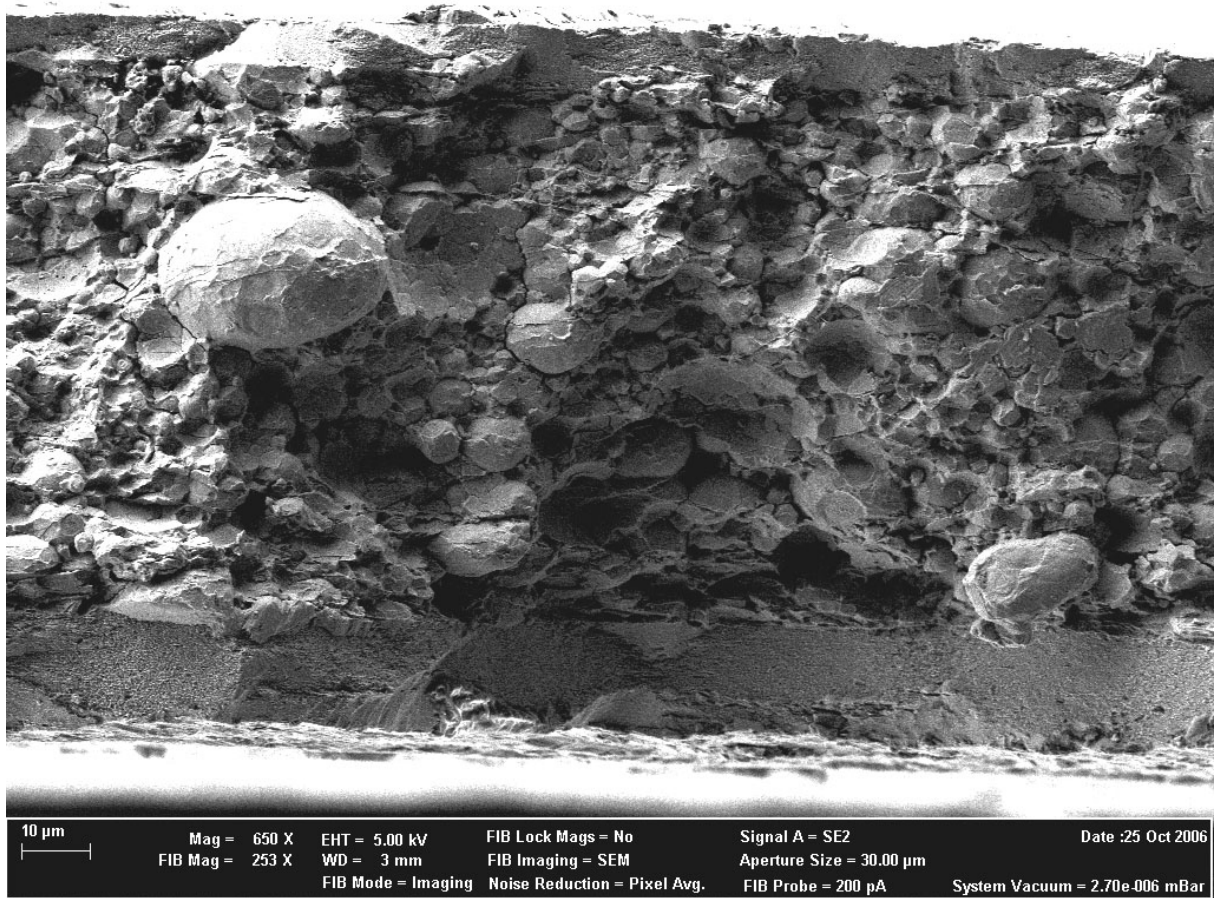


Fig. 8

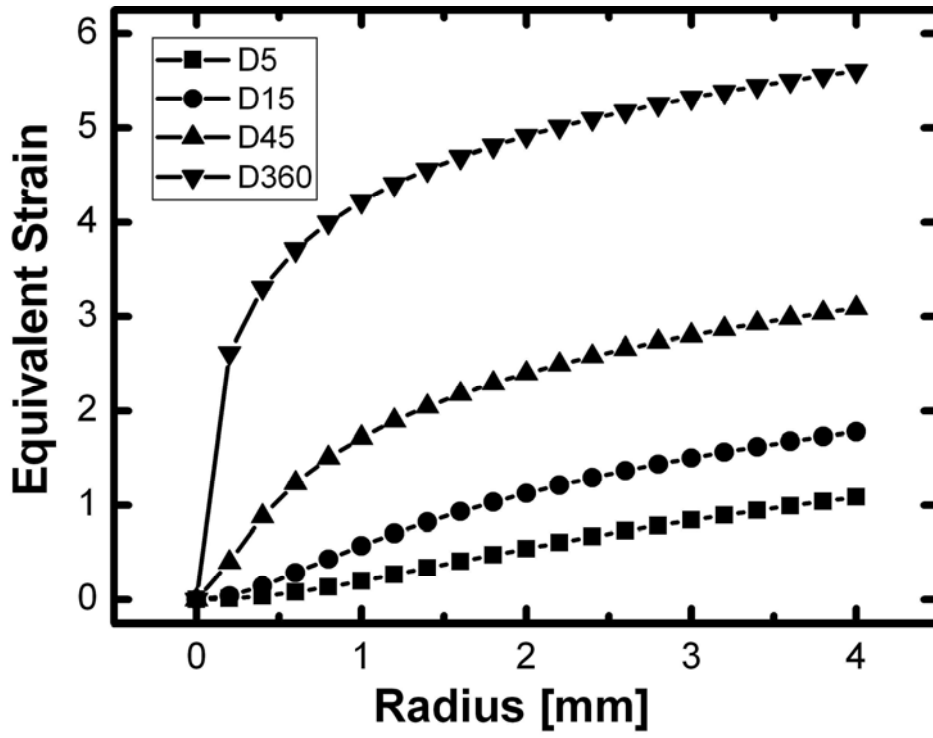


Fig. 9

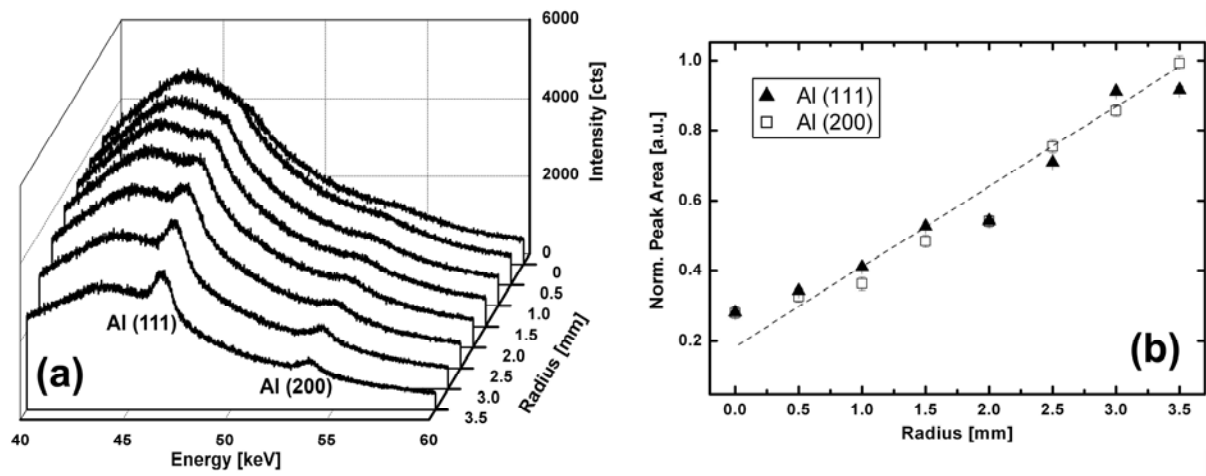


Fig. 10

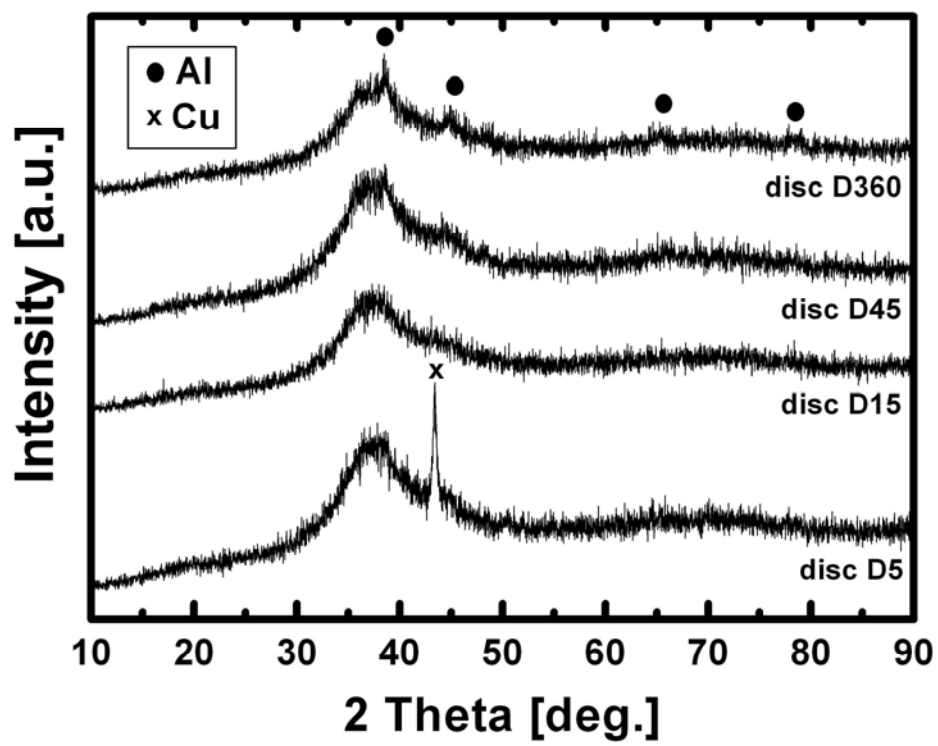


Fig. 11

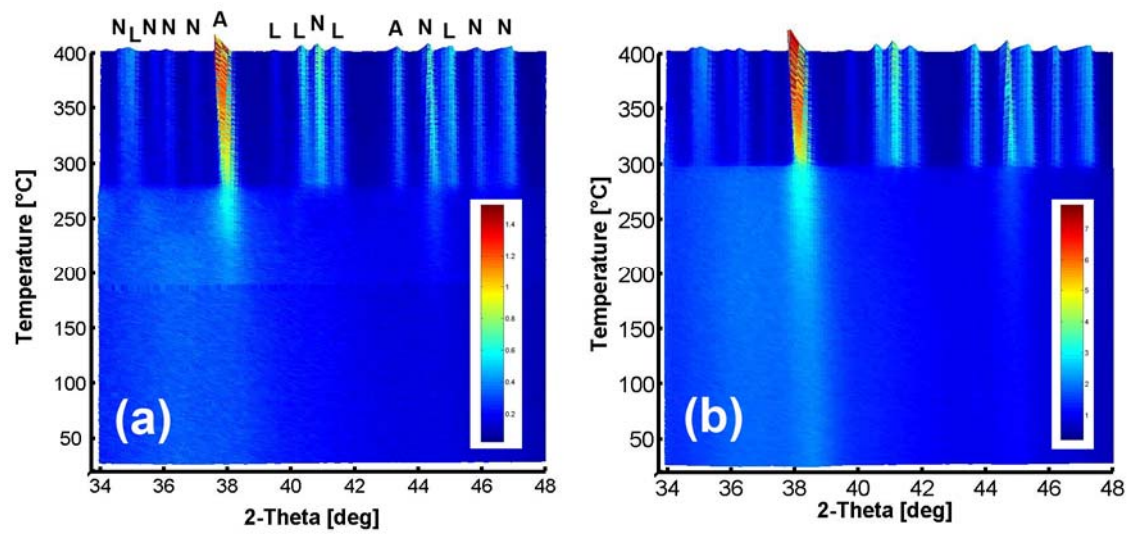


Fig. 12

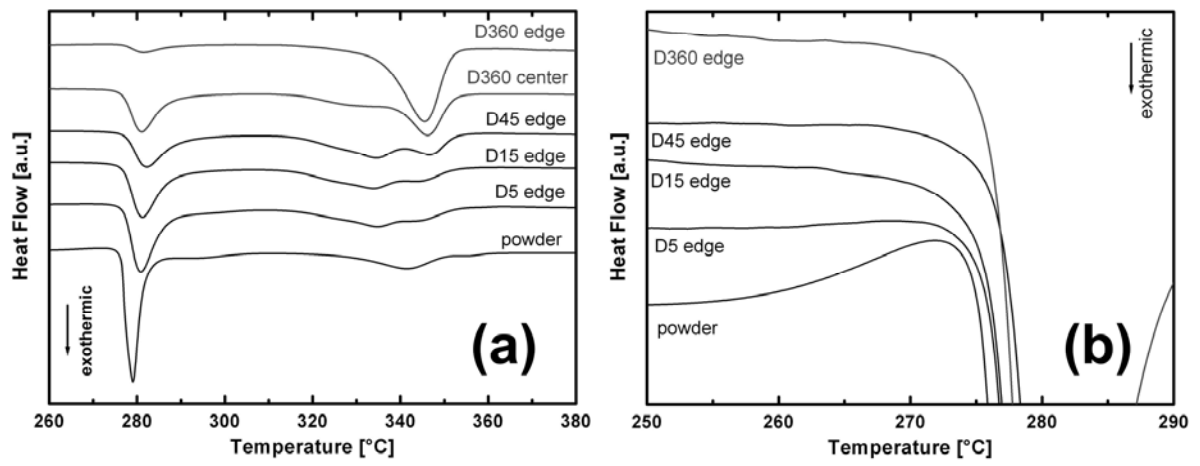


Fig. 13